PROCEEDINGS OF SCIENCE

Radio-gamma delay as signature of adiabatic expansion in blazar jets.

Andrea Tramacere,[a] **Vitalii Sliusar ,**[a] **Roland Walter ,**[a,*] **Jakub Jurysek** [a,b] **and Matteo Balbo**[a]

[a] *Department of Astronomy, University of Geneva, Chemin Pegasi 51, CH-1290 Versoix, Switzerland*

[b] *FZU - Institute of Physics of the Czech Academy of Sciences, Na Slovance 1999/2, 182 21 Praha 8, Czech Republic*

E-mail: andrea.tramacere@unige.ch, Roland.Walter@unige.ch

Geometrical constraints, specifically the alignment of relativistic jet with the observer's line of sight, make blazars the rarest and most powerful active galactic nuclei. They show extreme variability on different time-scales depending on the wavelength. Flares last from typical sub/few-hours in X-rays and TeVs, to months or years in the radio. Based on this observational evidence of radio-gamma delays with timescales ranging from weeks to months, we build, using the `JetSeT` framework, a self-consistent model of a relativistic expanding jet, taking into account all the radiative and accelerative processes acting in blazar jets. We present phenomenological predictions, validated by the numerical models, using a radio-gamma response profile including the delay, rising and decaying timescales, constraining expansion velocity and properties of the blob environment. We compare these predictions to results from temporal analysis of the BL Lacs object Mrk 421, finding a satisfactory agreement between the phenomenological trends and observations, and we derive constraints on the structure of the magnetic field and the location of the blazar zone.

38th International Cosmic Ray Conference (ICRC2023)
26 July - 3 August, 2023
Nagoya, Japan

*Speaker

PoS(ICRC2023)812

1. Introduction

Long-term multiwavelength (MW) campaigns for several blazars (BLs) have shown radio emission occurring with a significant delay with respect to the γ-ray band, with timescales ranging from weeks to years [6, 9]. This observational evidence is not compatible with different cooling timescales, and has been a matter of debate for several years. A possible interpretation was proposed by taking into account the different distances of the γ-ray and radio transparent region, with the moving region becoming transparent to the γ-rays [4] and later to the radio frequencies [3]. A key aspect to investigate in this scenario is to understand the role of the adiabatic expansion of the emitting region, and the consequences in terms of variation of the synchrotron self-absorption frequency (SSA), as presented in the seminal works by [7] and [18] and more recently, [8], [5] and [16]. In this paper, we report a summary of the most significant results presented in [16], based on the self-consistent numerical modelling of the adiabatic expansion of a relativistic blob, and the derivation of an inter-band response function, embedding the physical parameters of the model.

2. Model description for a leptonic plasma temporal evolution in an expanding blob.

We use the `JetTimeEvol` class from the `jet_timedep` module of the open-source `JetSeT`[1] framework [13–15], to follow the evolution of the emitting particle distribution under the effects of radiative cooling, adiabatic expansion, and acceleration processes (both systematic and stochastic), and to extract spectral energy distributions (SEDs) and light curves at any given time. The code proceeds through the numerical solution of a kinetic equation, following the same approach as in [15].

The baseline of our setup consists in reproducing an initial flaring stage (FS), followed by an expansion process happening during the long-term stage (LTS), within a leptonic synchrotron self-Compton (SSC) scenario. During the flare, particles are injected and accelerated in the acceleration region (AR) where they undergo both cooling and acceleration processes, and diffuse toward the radiative region (RR), where only losses take place (hereafter, all the quantities are expressed in the frame of the emitting blob, except for those labelled with the *obs* flag). The expansion process takes place in the RR region, at the time $t_{\rm exp}$. We follow the LTS evolution under the effects of radiative cooling and adiabatic expansion, with a duration of the simulation lasting long

[1] https://github.com/andreatramacere/jetset

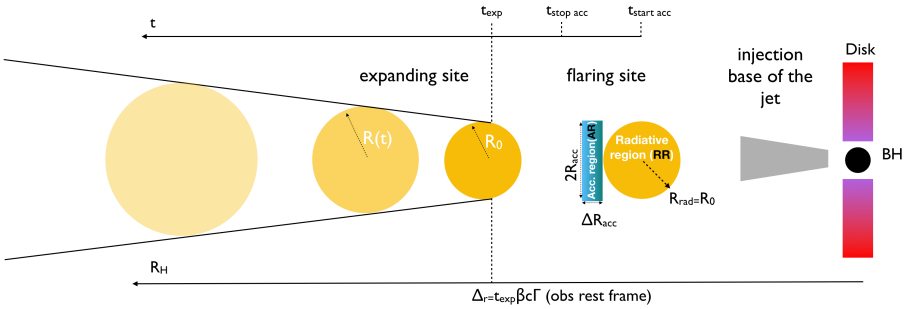

Figure 1: Schematic representation of the model implemented in `JetSeT`. At time $t_{\rm start\ acc}$, particles are injected and accelerated in the acceleration region where they undergo both cooling and acceleration processes and diffuse towards the radiative region, where only losses take place. The acceleration process ends at time $t_{\rm stop\ acc}$. After a time $t_{\rm exp}$, the expansion process takes place in the RR region. Figure adapted from [16].

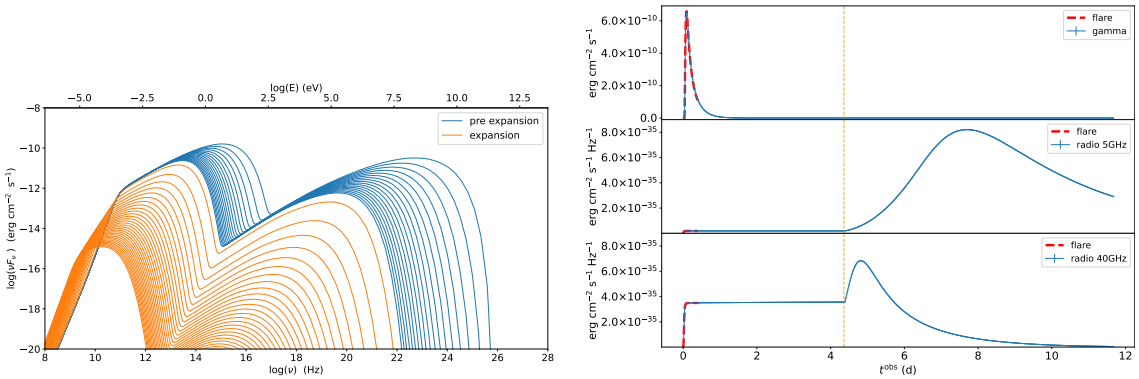

Figure 2: Simulation of an expansion episode, for $\beta_{\rm exp} = 0.1$. The *left panel* shows the evolution of the SEDs for the LTS, where the blue colour indicates to the pre-expansion stage, and orange indicates the expansion stage. The *right* panels show the merged light curves (FS and LTS) in the *Fermi*-LAT band, and at 5 and 40 GHz. The red dashed lines mark the light-curve segment belonging to the FS and the orange vertical dashed lines mark the beginning of the expansion in the LTS. An animated version of this simulation can be found on YouTube. Figure adapted from [16].

enough to follow the particle evolution due to the expansion process. A schematic representation of these processes is shown in Figure 1, and a detailed description of the model is presented in [16].The values of the magnetic field (B) and the radius (R) in the RR during the flaring episode are representative of the typical values obtained in the MW modelling for high energy peaked BL Lac (HBL) SEDs, and these values coincide with the initial values at the beginning of the expansion (B_0 and R_0). The evolution of $B(t) = B_0\left(\frac{R_0}{R(t)}\right)^{m_B}$ is dictated the flux freezing [2] according to m_B and $R(t) = R_0 + \beta_{\rm exp} c(t - t_{\rm exp})H(t - t_{\rm exp})$, from the beginning of the expansion process, assuming that the expansion begins at a time $t_{\rm exp}$, with a constant expansion velocity $\beta_{\rm exp} = v_{\rm exp}/c$, and that the particles are confined within the RR. Light curves are obtained by integrating SEDs between two frequencies, or as monochromatic.

3. Radio-γ response: phenomenological relations and validation against numerical simulations

A typical example, of a numerical simulation of a flaring episode followed by an expansion, is shown in Figure 2, for $\beta_{\rm exp} = 0.1$ and $t_{\rm exp} = 1 \times 10^7$ s. The SEDs evolution, for the post-flare non-expanding stage (left panel, blue lines), follows the usual pattern dictated by the radiative cooling timescales, whilst during the expanding-stage (orange lines) the evolution pattern changes. The most interesting effect is the evolution of the synchrotron component. On top of the flux decay dictated by the adiabatic losses and decreased magnetic field, we notice the shift in the SSA frequency, which is absent in the non-expanding stage. Whilst during the non-expanding stage the SSA is almost stable at the initial value of $\approx 10^{11}$ Hz, in the expanding stage, the SSA decreases with time according to $\nu^*_{\rm SSA}(t) = \nu^0_{\rm SSA}\left[\frac{R(t)}{R_0}\right]^{\phi}$ [16], where $\nu^0_{\rm SSA}$ is the SSA before the expanding stage, with $\phi = \frac{p+4}{m_B(p+2)+4}$ and p is the low-energy power-law index of the emitting electron distribution. The three right panels of Figure 2 show the light curves in the *Fermi*-LAT band, and at 5 and 40 GHz. For the case of the light curve, we show also the flaring episode (red dashed lines). During the post-flare non-expanding stage, the temporal behaviour is again in agreement with a purely radiative cooling without particle escape. On the contrary, in the expanding stage, the radio light

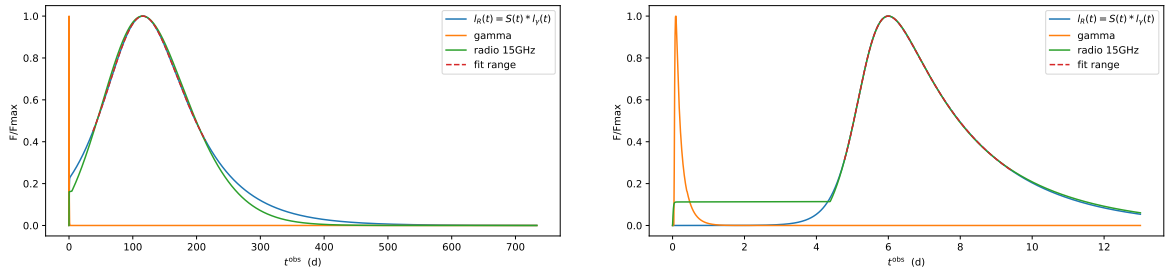

Figure 3: Convolution response, for two numerical simulations with the same parameters as in Figure 2, except $\beta_{exp} = 0.001$ (*left panel*) and $\beta_{exp} = 0.08$ (*right panel*). The red dashed line represents the actual fit interval, the orange line represents the γ-ray light curve in, the green line the 15 GHz radio light curve, and the blue line is the best fit of the radio light curve obtained from the convolution of the γ-ray light curve with the best-fit response. Figure adapted from [16].

curves increases in flux level when the expansion starts, with the time of the maximum happening earlier at larger frequencies (an animated version of this simulation can be found on YouTube). The delays and the different rise and decay times can be quantified using the phenomenological trends derived and validated in [16]. These trends, in the observer frame, as a function of the observed SSA in the expanding stage, $\nu^{*,obs}_{SSA}$, reads:

$$
\begin{aligned}
t^{obs}_{decay} &= \frac{R^{obs}_0}{m_B \beta_{exp} c}\left(\frac{\nu^{0,obs}_{SSA}}{\nu^{*,obs}_{SSA}}\right)^{\phi} \\
t^{obs}_{rise} &= \frac{1}{2}t^{obs}_{peak} = \begin{cases} \frac{1}{2}\frac{R^{obs}_0}{\beta_{exp} c}\left[\left(\frac{\nu^{0,obs}_{SSA}}{\nu^{*,obs}_{SSA}}\right)^{\phi} - 1\right] & \text{if } \nu^{0,obs}_{SSA} > \nu^{*,obs}_{SSA} \\ 0 & \text{otherwise} \end{cases} \\
\Delta t^{obs} &= t^{obs}_{exp} + t^{obs}_{peak} = t^{obs}_{exp} + \frac{R^{obs}_0}{\beta_{exp} c}\left[\left(\frac{\nu^{0,obs}_{SSA}}{\nu^{*,obs}_{SSA}}\right)^{\phi} - 1\right].
\end{aligned}
\tag{1}
$$

From a phenomenological standpoint, the radio light curves (l_R) can be interpreted as a convolution between the 'response' of the system and the γ-ray light curves (l_γ) [11, 12, 17] according to $l_R(t) = S(t) * l_\gamma(t)$. The response function proposed in [16] reads: $S(t) = A\frac{\exp\frac{-(t-\Delta t)}{t_f}}{1+\exp\frac{-(t-\Delta t)}{t_u}}$, i.e. the combination of a logistic function and an exponential decay. The scaling factor A depends mainly on the initial value of the Compton dominance, on the observed radio frequency, and on m_B. The decay time (t_f), the rise time (t_u), and the delay (Δt), are linked to the physical parameters of the blob by the phenomenological relations in Equation 1, whose actual derivation is presented in [16]. In Figure 3 we show an example of response application, to the 15 GHz radio light curve, for the two numerical simulations with the same parameters as in Figure 2, except $\beta_{exp} = 0.001$ (*left panel*) and $\beta_{exp} = 0.08$ (*right panel*). The value of β_{exp} impacts on t^{obs}_{decay}, t^{obs}_{rise} and Δt^{obs}, according to the trends in Equation 1.

Since the best-fit parameters of S depend on the physical parameters of the blob according to the trends in Equation 1, we can use these trends to infer the blob parameters. For example, we can use the long-term numerical simulations, with $\beta_{exp} = 0.1$, and, for a given set of frequencies, we can determine the best fit response $S(t)$ parameters. In this way, we will collect for t^{obs}_{decay}, t^{obs}_{rise} and Δt^{obs}, a set of values corresponding to each frequency, and finally, we can fit these set of values against the

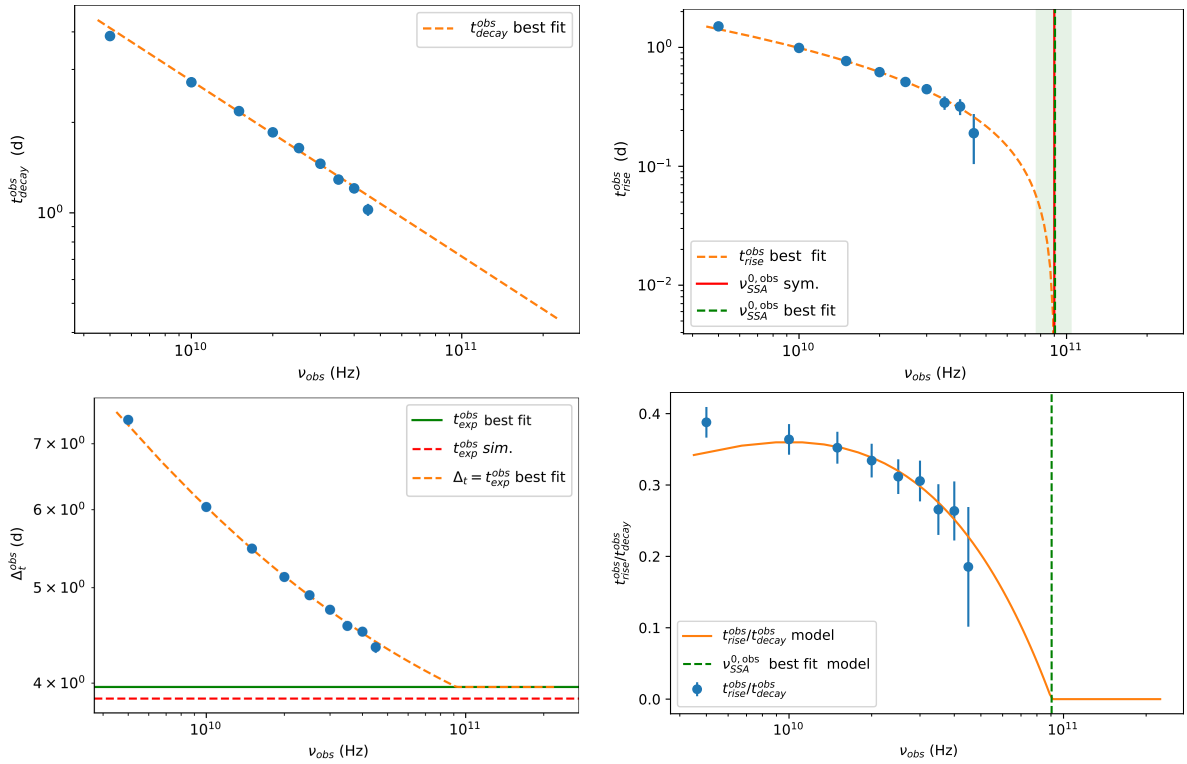

Figure 4: Expanding trends for ν obtained from the simulations. *Top left panel*: Decay times (blue solid points) obtained from the best fit for the radio-γ response, for the simulation with $\beta_{\rm exp} = 0.1$ and ranging $\nu_{\rm obs} = [5, 45]$ GHz. The orange dashed line represents the best fit with first equation of Equation 1. *Top right panel*: Same as in the top left panel, but for the case of $t^{\rm obs}_{\rm rise}$. The dashed line corresponds to the best fit with the second equation of Equation 1. *Bottom left panel*: Same as in the top left panel, but for $\Delta t^{\rm obs}$. The dashed line corresponds to the best fit with the third equation of Equation 1. *Bottom right panel*: Trend of $t^{\rm obs}_{\rm rise}/t^{\rm obs}_{\rm decay}$ as observed in the simulations (solid blue points) compared to the expectation from the individual best-fit trends of $t^{\rm obs}_{\rm rise}$ and $t^{\rm obs}_{\rm decay}$ (dashed line). Figure adapted from [16].

predictions from Equations 1. The results are shown in Figure 4, and the best-fit results are reported in Table 1. For the decay trend (top left panel), we find $R^{\rm obs}_0 \simeq 1.7 \times 10^{14}$ cm, corresponding to a blob frame value of $R_0 \simeq 5.1 \times 10^{15}$ cm, which is in good agreement with the simulation value. The best-fit value of $\nu^{0,\rm obs}_{\rm SSA} = 100 \pm 20$ GHz is compatible with that measured in the simulated SEDs. Both the estimate of $\beta_{\rm exp} = 0.09 \pm 0.01$ and the estimate of $m_B = 1.0 \pm 0.1$ are in excellent agreement with the simulation values. The $t_{\rm rise}$ trend (top right panel of Figure 4) returns a value of $R^{\rm obs}_0 = 2.4 \pm 1.0 \times 10^{14}$, which is $\approx 60\%$ larger than the simulation value, but still compatible within one sigma. The $\beta_{\rm exp} = 0.03 \pm 0.01$ is significantly lower than the simulated one. The value of $\nu^{0,\rm obs}_{\rm SSA} \simeq 90 \pm 10$ provides a very good estimate of the simulation value $\nu^{0,\rm obs}_{\rm SSA} = 90$ GHz. In the top right panel of Figure 4, the green shaded area shows the 1-σ interval from the best fit, and the vertical red solid line represents the simulation value. The delay trend (bottom left panel of Figure 4) returns an estimate of $\beta_{\rm exp} = 0.06 \pm 0.01$, which is $\approx 40\%$ lower than the simulation value, and an estimate of $\nu^{0,\rm obs}_{\rm SSA} \simeq 90 \pm 10$ GHz, which is in agreement with the simulation value. In this case, we also estimate the value of $t^{\rm obs}_{\rm exp} = (3.4 \pm 0.1) \times 10^5$ s with good accuracy, which is in agreement

		actual values		values from ν trend best fit		
		blob	obs	$t^{\rm obs}_{\rm rise}$	$t^{\rm obs}_{\rm decay}$	$\Delta t^{\rm obs}$
R_0	cm	5×10^{15}	1.66×10^{14}	$(2.4 \pm 1.0) \times 10^{14}$	$(1.7 \pm 0.2) \times 10^{14}$	$(1.6 \pm 0.1) \times 10^{14}$
$\nu^0_{\rm SSA}$	GHz	3	90	90 ± 10	100 ± 20	90 ± 10
$t_{\rm exp}$	s	1×10^7	3.3×10^5			$(3.4 \pm 0.1) \times 10^5$
m_B		1			1.0 ± 0.1	
$\beta_{\rm exp}$	c	0.1		0.03 ± 0.01	0.09 ± 0.01	0.06 ± 0.01
ϕ				0.24 ± 0.07	0.58 ± 0.02	0.50 ± 0.02
p		1.46		0.6 ± 0.2	1.7 ± 0.1	1.4 ± 0.1

Table 1: Best fit results, for the $\nu_{\rm obs}$ simulations of the trends reported in Equation 1 for $t^{\rm obs}_{\rm rise}$, $t^{\rm obs}_{\rm decay}$, and $\Delta t^{\rm obs}$, and shown in the top left, top right, and bottom left panels of Figure 4, respectively. The parameter p, i.e. the electron distribution spectral index, is evaluated from the best-fit parameters using the second equation of Equations 8 in [16].

with the simulation value within a few percent. Finally, we comment on the effect of the initial SSA frequency on the rising time. As already noted, the rising time decreases to zero as $\nu^*_{\rm SSA}$ approaches $\nu^0_{\rm SSA}$. This implies that even if we obtain a long decay time because of the low expansion rate, we might expect a short rising time if $\nu^*_{\rm SSA}$ is close to $\nu^0_{\rm SSA}$. As in the case of the $\beta_{\rm exp}$ trends, we estimate the electron distribution index p from the best-fit parameters using the second equation of Equations 8 in [16]. The agreement with the simulation value is lower than in the case of the $\beta_{\rm exp}$ trends, in particular for the case of the rise time trend, but nevertheless both delay and decay times provide an estimate that is consistent within one sigma with the simulation value.

4. Application of the radio-γ response to observational data for Mrk 421.

As a final step, we applied the response and the phenomenological trends discussed above to real data from *Fermi*-LAT [1] (in the 1-300 GeV band) and from the OVRO radio telescope [10] for Mrk 421 (see [16] for details on *Fermi*-LAT light-curve extraction). The left panel of Figure 5 shows the results of the best-fit response obtained by minimising, over a 7.5-year period (MJD 55500-58226), the deviations between the observed radio light curve and the synthetic light curve obtained by the convolution of the *Fermi*-LAT daily binned light curve with the response $S(t)$, discussed above. The *Fermi*-LAT light curve starts about two years before the period used for the minimisation to account for the long-lasting effect of the response, particularly $\Delta t^{\rm obs}$. The observed GeV and radio and the resulting synthetic radio light curves are shown in the left panels of Figure 5, and resulted in a $\Delta t^{\rm obs} = 37.58^{+0.13}_{-0.13}$, $t^{\rm obs}_{\rm rise} \lesssim 1$ day, and $t^{\rm obs}_{\rm decay} = 126.5^{+1.3}_{-1.3}$ days. The synthetic light curve reproduces the long-term trend, with short-term deviations possibly hinting for a change in the intensity of the response (e.g. the non-constant scaling factor A, or a change in the beaming factor due to a bending jet), or possible different origin of single flares, as for the case of the fast radio flare near MJD 56897 and a wider flare at about MJD 55600 (see Figure 5). As the response rise time is similar to the binning time of the GeV light curve, its value indicates a rising time shorter than one day.

The physical insight, embedded in the convolution analysis, can be revealed using a Monte Carlo Markov Chain (MCMC) approach, defining a composite log-likelihood $\mathcal{L} = \mathcal{L}_{\rm rise} + \mathcal{L}_{\rm decay} + \mathcal{L}_{\rm delay}$, where $\mathcal{L}_{\rm rise}$, $\mathcal{L}_{\rm decay}$, and $\mathcal{L}_{\rm delay}$ represent the log-likelihood functions corresponding to rise, decay,

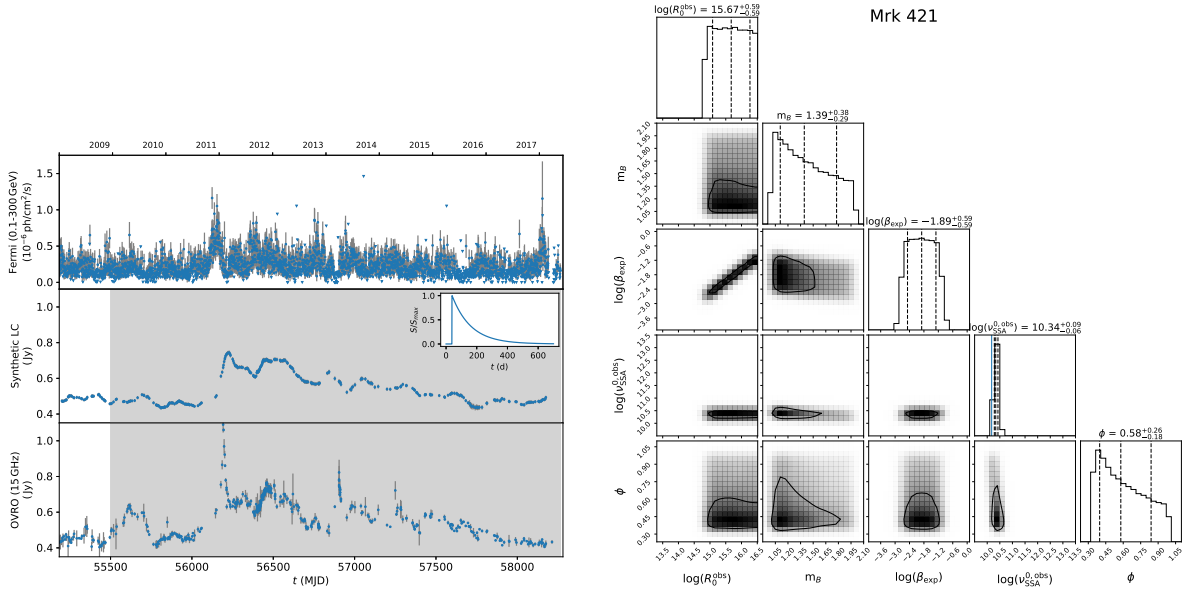

Figure 5: *Left panel:* synthetic radio light curve for Mrk 421 (middle) created as a convolution of the daily-binned *Fermi*-LAT 0.1-300 GeV light curve (top) and of the radio response (inset panel), compared with the OVRO 15 GHz radio light curve (bottom). Fitting time range is highlighted in grey. *Right panel:* posterior distribution for a MCMC sampling of the composite log-likelihood for rise, decay, and delay time in Equation 1. To sample the parameter space, we use uninformative flat priors, with $m_B \in [1, 2]$, $\phi \in [1/3, 1]$, $\nu^{0,\rm obs}_{\rm SSA} \in [10, 10^4]$ GHz, $\beta_{\rm exp} \in [10^{-4}, 1]$. The range of $R^{\rm obs}_0$ is determined by setting a flat range for the observed γ-ray variability timescale $t^{\rm var}_\gamma \in [0.25, 14]$ days, and setting $R^{\rm obs}_0 = t^{\rm var}_\gamma c$, corresponding to $R^{\rm obs}_0 \in [6.5 \times 10^{13}, 3.6 \times 10^{17}]$ cm. The solid black line identifies the 1-σ containment for a bivariate Gaussian distribution. On the diagonal, we plot the marginalised posterior distributions, and with the vertical dashed black lines we indicate the 0.16, 0.5, and 0.84 quantiles. The blue vertical line in the $\log(\nu^{0,\rm obs}_{\rm SSA})$ histogram identifies the 15 GHz observed OVRO frequency. On top of each marginalised histogram we report the confidence level corresponding to the quantiles. Figure adapted from [16].

and delay time in Equation 1 (see [16] for more details). The right panel of Figure 5 shows the sampler results, providing informative confidence regions for the parameters of interest, except for $\log(R^{\rm obs}_0)$ where we notice a flat posterior for $\log(R^{\rm obs}_0) = 15.67^{+0.59}_{-0.59}$. The magnetic index $m_B = 1.39^{+0.38}_{-0.29}$ has the peak of the probability density function at $m_B = 1$. The low value of $\log(\nu^{0,\rm obs}_{\rm SSA})$, corresponding to $\nu^{0,\rm obs}_{\rm SSA} \approx 22$ GHz, is compatible with the short $t^{\rm obs}_{\rm rise}$ returned by the convolution analysis, and very close to the observed OVRO frequency of 15 GHz. The posterior confidence level of the index ϕ implies $p = 1.97^{+1.26}_{-0.72}$, a value compatible with the predictions from Fermi first-order acceleration plus a stochastic component, which is in agreement with previous theoretical and observational analyses [14, 15].

5. Conclusions

We presented a summary of the most significant results, regarding the signatures of adiabatic expansion in radio-γ delays, observed in blazar jets [16]. The presence of adiabatic expansion implies delays between the radio and the γ-ray emission, due to the shift of the SSA frequency, with the delay, rising, and decaying timescales depending on the velocity of the expansion and on the time required for the source to exhibit an SSA frequency below the observed radio frequency. The inter-band response function, embedding the aforementioned parameters, was applied to radio and

γ-ray light curves of Mrk 421 providing a satisfactory agreement on the long-term variability, and by using a MCMC sampler returned the estimate of some relevant physical parameters of the jet. We aim to extend the presented analysis to polarization measurements and to jet collimation profile kinematics, in order to investigate how relativistic jets in blazars form and develop, to understand the transition from the kinematically to the magnetically dominated regime, and to possibly identify extra variability patterns due, for example, to a bending jet, and the connection with the localization of the high-energy flaring site, where the particle acceleration occurs. The work presented here is fully reproducible by following the instructions in the git repository[2], and a detailed description of the analysis can be found in the JetSeT YouTube channel.

References

[1] Atwood W. B., et al., 2009, ApJ, 697, 1071
[2] Begelman M. C., Blandford R. D., Rees M. J., 1984, Rev. Mod. Phys., 56, 255
[3] Blandford R. D., Königl A., 1979, ApJ, 232, 34
[4] Blandford R. D., Levinson A., 1995, ApJ, 441, 79
[5] Boula, S. Mastichiadis, A. 2022, A&A, 657, A20
[6] Max-Moerbeck W., et al., 2014, MNRAS, 445, 428
[7] McCray R., 1969, ApJ, 156, 329
[8] Potter W. J., 2018, MNRAS, 473, 4107
[9] Pushkarev A. B., Kovalev Y. Y., Lister M. L., 2010, ApJ, 722, L7
[10] Richards J. L., et al., 2011, ApJS, 194, 29
[11] Sliusar V., et al., 2019a, in High Energy Phenomena in Relativistic Outflows VII. p. 32 (arXiv:1909.13106)
[12] Sliusar V., et al., 2019b, in 36th International Cosmic Ray Conference (ICRC2019). p. 796 (arXiv:1908.09770)
[13] Tramacere A., 2020, JetSeT: Numerical modeling and SED fitting tool for relativistic jets (ascl:2009.001)
[14] Tramacere A., Giommi P., Perri M., Verrecchia F., Tosti G., 2009, A&A, 501, 879
[15] Tramacere A., Massaro E., Taylor A. M., 2011, The Astrophysical Journal, 739, 66
[16] Tramacere A., Sliusar V., Walter R., Jurysek J., Balbo M., 2022, A&A, 658, A173
[17] Türler M., Courvoisier T. J.-L., Paltani S., 1999, A&A, 349, 45
[18] van der Laan H., 1969, in Quasars and high-energy astronomy. p. 49

[2] https://github.com/andreatramacere/adiabatic_exp_radio_gamma_delay